magnetochemistry

MDPI

Article

Controllable Synthesis of Magnetic Composite Derived from MIL-88D and Study on Adsorption Properties of Cu^{2+}

Zhongyuan Zheng [1], Jinshan Yu [1], Ling Jiang [1], Jiacheng Zhang [1] and Min Lu [2,*]

[1] State Grid Tianjin Electric Power Company Electric Power Science Research Institute, Tianjin 300220, China; popceol@163.com (Z.Z.); pinfan10@126.com (J.Y.); 18722591775@163.com (L.J.); 18844215351@163.com (J.Z.)
[2] School of Chemical Engineering, Northeast Electric Power University, Jilin 132000, China
* Correspondence: lumin19770919@163.com; Tel.: +86-1357-851-1861

Abstract: In this paper, MIL-88D (Fe) with spindle shape was prepared by the hydrothermal synthesis method, a metal oxide with a new structure was obtained by calcination at different temperatures as a precursor, and a magnetic iron oxide composite was prepared successfully. At the same time, it was used as an adsorption material for the adsorption of heavy metal ions Cu^{2+}. The influence of the initial pH value and adsorption time on the adsorption effect was investigated, the adsorption kinetics and adsorption isotherm were further fitted, and the adsorption mechanism was preliminarily analyzed. The results show that the magnetic iron oxide composites have a good adsorption capacity for Cu^{2+}. The pH value is an important parameter that affects the adsorption effect. The adsorption of Cu^{2+} by magnetic iron oxide composites reached adsorption equilibrium in 30 min. The adsorption of Cu^{2+} by magnetic iron oxide composites conforms to the second-order reaction kinetics and Langmuir adsorption isotherm equation, which indicates that the adsorption process mainly occurs through chemisorption and typical single-molecular-layer adsorption.

Keywords: MIL-88D; composite material; Cu^{2+}; adsorb

check for updates

Citation: Zheng, Z.; Yu, J.; Jiang, L.; Zhang, J.; Lu, M. Controllable Synthesis of Magnetic Composite Derived from MIL-88D and Study on Adsorption Properties of Cu^{2+}. *Magnetochemistry* **2024**, *10*, 64. https://doi.org/10.3390/magnetochemistry10090064

Academic Editor: Carlos J. Gómez García

Received: 25 July 2024
Revised: 17 August 2024
Accepted: 29 August 2024
Published: 31 August 2024

Copyright: © 2024 by the authors. Licensee MDPI, Basel, Switzerland. This article is an open access article distributed under the terms and conditions of the Creative Commons Attribution (CC BY) license (https://creativecommons.org/licenses/by/4.0/).

1. Introduction

In recent years, the rapid improvement of industrial production has led to increasingly serious environmental problems, and the water resources closely related to human survival have suffered unimaginable damage [1]. As we all know, heavy metal ions, as one of water resources' pollutants that can not be ignored, not only cannot be biodegraded but can also accumulate in the biological body and bring a variety of diseases, which has a great impact on economic development, ecological environment destruction, and human survival. Therefore, the effective removal of heavy metal ions has become one of the main problems to be solved urgently in terms of current water pollution [2,3]. At present, the methods of heavy metal ion pollution mainly include precipitation, electrolysis, coagulation, membrane separation technology, reverse osmosis, adsorption, etc. Among them, the adsorption method is widely used due to its advantages of simple operation, being low cost, being green and harmless, and having a good removal effect [4,5].

The most important thing in the adsorption method is to select a suitable adsorbent with a large adsorption capacity and fast adsorption rate. At present, the practical application of the commonly used adsorbents is severely limited by their low adsorption rates and adsorption capacity. Compared with common natural minerals, cellulose, commercial activated carbon, and other adsorption materials, nanomaterials have a high specific surface area, rapid dispersion, rapid reaction, and strong adsorption characteristics brought about by surface effects, and quantum and dielectric effects brought about by their discontinuity [6,7]. The synthesis of new nano-structured adsorbent materials and their application in water pollution control have become one of the hot spots in the field of environmental functional materials. Among them, the nano-porous carbon material has a high specific

surface area, adjustable pore structure, and extremely fast adsorption rate. The adsorption forms of physical adsorption and chemical adsorption are the most widely used in water treatment. The most common method for preparing nanoporous carbon materials is to decompose organic precursors at a high temperature and then activate them by physical and chemical methods.

Metal–organic frameworks (MOFs) are a kind of crystalline porous material with a periodic special network structure formed by the self-assembly of inorganic metal centers (metal ions or metal clusters) and bridling organic ligands [8–10]. They have both the rigidity of inorganic materials and the flexibility of organic materials, and have attracted much attention due to their advantages such as large specific surface areas, multiple adsorption sites, and strong designability [11,12]. However, the durability and stability of most traditional MOFs in aqueous solution are poor, which destroys the coordination of the MOFs, replaces the attached ligand, blocks the binding site, prevents the adsorption of other target molecules, and may lead to the structural collapse, seriously hindering the direct practical application of MOFs. In recent years, researchers have found that derivatives prepared with MOFs as precursor systems have the characteristics of highly controllable structures and functions and high specific surface areas and porosity, and are potential excellent adsorption materials for water treatment. In addition, the organic ligands in MOFs contain a large number of carbon elements, so appropriate organic ligands and metal ions can be selected to prepare MOFs, and through direct carbonization, MOFs can be transformed into nano-ordered porous carbon materials with different components, pore structures, and surface chemical environments [13]. Yurou Feng et al. successfully synthesized a highly efficient Cu^{2+} adsorbent using Ca^{2+} as a crosslinking agent through in situ self-assembly from ZIF-8@ALG complex hydrogel [14]. Dan Xu et al. synthesized ZIF-67 composite SiO_2 material (ZIF-67@SiO_2) using ethyl orthosilicate (TEOS) as a silicon source, and carried out one-step carbonization with ZIF-67@SiO_2 as a carbon precursor to prepare magnetic porous nitrogen-doped carbon material (MNPC@SiO_2). Subsequently, the Ce^{3+} composite P-MNPC@SiO_2 was obtained by the functionalization of diethylphosphine triethoxysilane (DPTS) [15].

Suitable adsorption materials in the treatment of heavy metal wastewater are not only required to have good adsorption performance, but also it to be easy to achieve solid–liquid separation after adsorption, otherwise they will cause material waste and even secondary pollution. At present, due to its special reactivity, surface/interface properties, magnetic properties, excellent specific surface area, and pore structure, iron oxide shows excellent adsorption ability for contaminated metal ions, and many scholars have modified or magnetized existing adsorbents to solve the above problems [16,17]. Wei et al. successfully synthesized α-Fe_2O_3 with a special hollow nest shape and applied it to the adsorption of heavy metal ions. The results show that it exhibits an excellent adsorption capacity for As^{5+} and Cr^{6+}, with adsorption capacities of 75.3 mg/g and 58.5 mg/g, respectively, mainly due to its unique porous structure and specific surface area [18]. Huang et al. used a regular spherical iron oxide with an unsmooth surface to adsorb Cu^{2+} in water, and the results showed that its maximum adsorption capacity was 13.44 mg/g [19].

In this paper, MIL 88D (Fe) with a spindle shape was prepared by the hydrothermal synthesis method, which can not only maintain the topological structure and increase the volume of the material, but also facilitate mass transfer under polar conditions such as aqueous solution. At the same time, the iron-based MOFs with iron as their center have low toxicity and good environmental compatibility. On this basis, the porous carbon materials with a large specific surface area and controllable pore size/morphology were obtained by composite aggregation and carbonization using rich organic ligands as carbon sources. This overcomes the shortcomings of the poor self-stability of pure MOF material and the unsatisfactory adsorption effect of the liquid phase. At the same time, the central metal ion of MIL 88D (Fe) is embedded in the carbon matrix during the carbonization process and forms a magnetic metal oxide Fe_3O_4, which not only promotes synergies with the electron transfer of carbon, but also facilitates the rapid separation of adsorbent under the

action of an external magnetic field. Furthermore, the composition and structure of the synthetic materials were characterized by XRD and SEM. Taking Cu^{2+} as the adsorption object, the influencing factors of the pH value and adsorption time of the adsorption system on the adsorption effect of the composite derived from MIL 88D was investigated, and the adsorption mechanism was preliminarily explored.

2. Materials and Methods

2.1. Instruments and Reagents

X-ray powder diffraction (XRD, XRD-7000 X, shimadzu Co., LTD., Kyoto Japan) was used to obtain the diffraction pattern of the phase composition of the sample. The elemental electronic structure and valence state of the material's surface were revealed via X-ray photoelectron spectroscopy (XPS, Thermo Scientific K-Alpha, Waltham USA) employing Al Kα radiation. Raman spectra were recorded using a Horiba Scientific LabRAM HREvolution with a 532 nm laser source. Fourier infrared spectroscopy (FT-IR) was used to detect the characteristic chemical bonds of the samples. Scanning electron microscopy (SEM, XL-30 FEG, FEI Company, State of Oregon USA) was used to analyze the surface morphology of materials; specific surface area (BET, ASAP 2020, Mack Instruments, Atlanta USA) and pore size distribution were used to measure the structural characteristics of the sample. Determination of Cu^{2+} concentration of heavy metal ions was conducted by atomic absorption spectrophotometer (AA-7000A, Shimadzu Co., LTD., Kyoto Japan).

All reagents in this paper are analytically pure and have not been further purified.

2.2. Preparation of MIL-88D and Its Derived Carbon Coated Iron Oxides

By ultrasonic dispersion, 540 mg (2 mmol) of $FeCl_3 \cdot 6H_2O$ was uniformly dispersed into 30 mL of N, n-dimethylformamide (DMF) to obtain solution A; solution B was prepared by dispersing 242 mg (1 mmol) of 4,4′-biphenyl dicarboxylic acid uniformly into DMF of 30 mL; then, solution A was added to solution B drop by drop in continuous ultrasound, the ultrasonic state was maintained until the dispersion was uniform after the drip was finished, and solution C was prepared. Solution C was transferred to the reactor of 100 mL for solvothermal reaction at 120 °C for 48 h and cooled to room temperature after the reaction. The resulting solution was centrifuged (5000 r/min, 3 min) and washed with DMF and anhydrous ethanol three times, respectively. After drying, orange powder was obtained, that is, MIL-88D.

The obtained MIL-88D was calcined under N_2 atmosphere at 700 °C for 2 h with a temperature rise rate of 5 °C/min as the precursor. After calcination, the derivative porous carbon-coated iron oxide composite material was obtained, denoted as Fe_3O_4@C.

2.3. Cu^{2+} Adsorption Experiment

The pH of the test solution was adjusted with 0.1 mol/L HCl and 0.1 mol/L NaOH. All adsorption experiments were carried out on a constant temperature oscillator at 250 r/min at 25 °C, and the amount of adsorbent was maintained at 1.0 g/L. Under a certain pH value, $CuSO_4$ solution with a mass concentration of 50 mg/L (C_0, mg/L) was taken as the research object, and a certain amount of MIL-88D-derived magnetic iron oxide composite material (m, mg) was added to 20 mL Cu^{2+} solution (V, L), which was separated by external magnetic force after mechanical stirring for a certain time. The concentration of metal ions at different times was determined to explore the adsorption kinetics. The residual Cu^{2+} content (C_t, mg/L) was determined by atomic absorption spectrophotometer with appropriate supernatant, and the adsorption rate A (%) and adsorption amount Q (mg/g) were calculated according to Equations (1) and (2), respectively.

$$A = 100 \times (C_0 - C_t)/C_0 \quad (1)$$

$$Q = (C_0 - C_t) \times V/m \quad (2)$$

2.4. Reuse Experiment

The Fe_3O_4@C composite magnetic porous carbon material after adsorbing copper ions in the previous step was used for magnetism. It was separated from solid and liquid, then washed with 1 M EDTA solution, washed three times, and then washed with deionized water until neutral to complete recovery. After recovery, the adsorption property of Fe_3O_4@C composite magnetic porous carbon material was tested five times, and the reuse value of Fe_3O_4@C composite magnetic porous carbon material was explored. After adsorption, the amount of iron ions dissolved in the solution was also measured by atomic absorption spectrophotometer.

3. Results and Discussion

3.1. Sample Preparation and Characterization

Figure 1 shows the XRD patterns of MIL-88D and the derived porous carbon-coated iron oxides (Fe_3O_4@C). First, the results for the synthesized MIL-88D were completely consistent with the reported MIL-88D characteristic peak location, indicating its successful synthesis (Figure 1a) [20]. In Figure 1b, Fe_3O_4@C has obvious characteristic peaks at 2θ = 30.2°, 35.5°, 43.2°, 53.6°, 57.1°, and 62.7°, and these peaks all exhibit narrow and sharp characteristics. These correspond to the crystal faces (220), (311), (400), (422), (511), and (440) in the Fe_3O_4 standard card (JCPDS No. 88-0315). It is worth noting that no other peaks appear except Fe_3O_4, that is, no obvious C-characteristic peak can be detected in XRD, which suggests that C exists in an amorphous state.

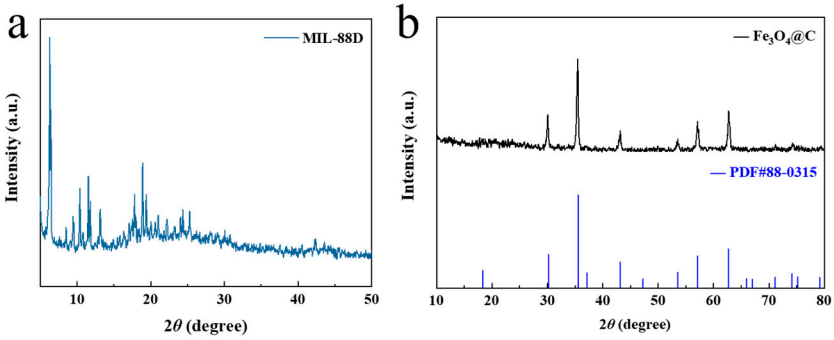

Figure 1. XRD patterns of (**a**) MIL-88D and (**b**) Fe_3O_4@C.

XPS can characterize the chemical composition and valence state chemical state of the materials surface. In Figure 2a, the survey spectrum of the Fe_3O_4@C composite exhibits Fe 2p, O 1s, and C 1s peaks, which are in good agreement with the composition of Fe_3O_4@C. The C 1s spectrum shows that C has both sp^2 and sp^3 forms, and the two peaks at 286.1 eV and 288.6 eV represent some of the residual organic ligands after pyrolysis (Figure 2b). In Figure 2c, the peaks at 529.7 eV and 531.8 eV belong to the Fe-O bond and oxygen vacancies (*V*o) in Fe_3O_4, respectively. The peak at 533.2 eV indicates O in the residual organic material. As shown in Figure 2d, the Fe element mainly consisted of two valence states of "+2" (709.7 eV and 722.8 eV) and "+3" (711.0 eV and 724.1 eV), which correspond to the valence state that Fe is supposed to have in Fe_3O_4.

Raman spectroscopy is an effective characterization technique for analyzing carbon materials. As shown in Figure 3a, the peaks at 1350 and 1580 cm^{-1} are the D and G peaks, respectively, for carbon materials. The D peak originates from sp^3-C in amorphous carbon, while the G peak represents sp^2-C in graphitic carbon. The above results indicate that Fe_3O_4@C contains both sp^3-C and sp^2-C. In addition, the intensity ratio of the D and G peaks (I_D/I_G) can reflect the degree of graphitization of the carbon materials. After fitting, the I_D/I_G value of Fe_3O_4@C is calculated to be 1.25, indicating a low degree of graphitization. This is also consistent with the absence of diffraction peaks of graphitic carbon in the XRD pattern.

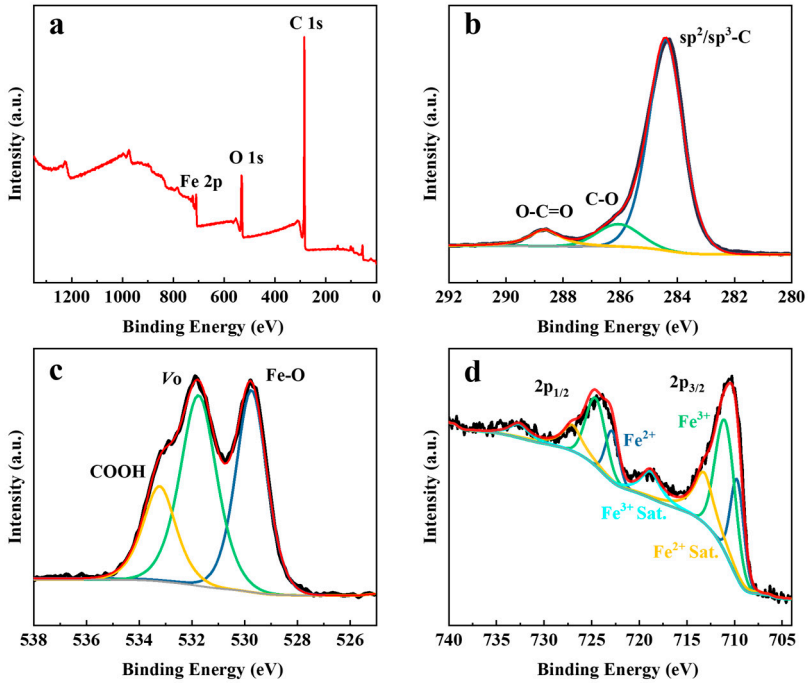

Figure 2. XPS spectra of Fe_3O_4@C: (**a**) survey spectrum, (**b**) C 1s, (**c**) O 1s, and (**d**) Fe 2p.

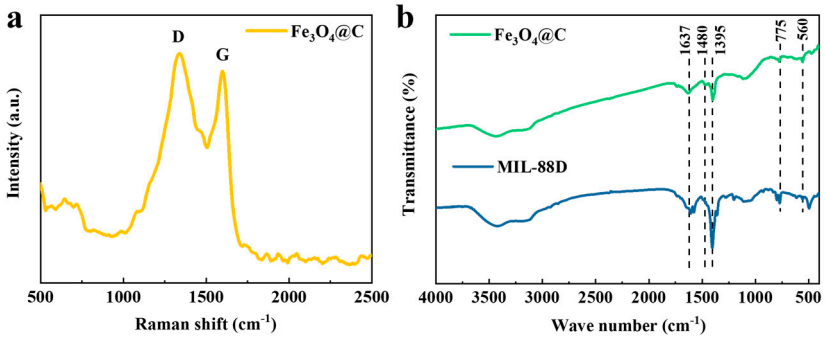

Figure 3. (**a**) Raman spectra of Fe_3O_4@C; (**b**) FT-IR spectra of MIL-88D and Fe_3O_4@C.

In order to prove the presence of carbon in the products and the structural changes in the materials before and after calcination, Fourier infrared spectroscopy analysis was performed on the two materials. The results are shown in Figure 3b. Compared with the precursor of MIL-88D, the Fe-O vibration peak at 560 cm^{-1} appeared in the carbon-coated iron oxide. This indicates the presence of iron oxides in the products after high-temperature calcination [21]. In addition, the peak at 1395 cm^{-1} corresponds to the C-C absorption peak, and the absorption peaks at 1480 cm^{-1} and 1637 cm^{-1} correspond to the stretching vibration of C=C and C=O, respectively [22]. It is not difficult to find that, compared with MIL-88D, the product after high-temperature calcination still has obvious C=C, C=O, and C-C characteristic diffraction peaks, which also confirms the existence of carbon in the product after high-temperature calcination.

MIL-88D and its derived carbon-coated iron oxide composites were characterized by scanning electron microscopy, and the results are shown in Figure 4. MIL-88D is a spindle as a whole, and after high-temperature treatment, Fe_3O_4@C basically maintains the spindle structure, although some of the spindles are destroyed and collapsed, and the surface is uniformly covered with dense small protrusions, showing obvious folds as a whole. For Fe_3O_4@C, the surface full of folds contributes to the increase in its specific surface area, and also reflects the characteristics of its pore structure to a certain extent.

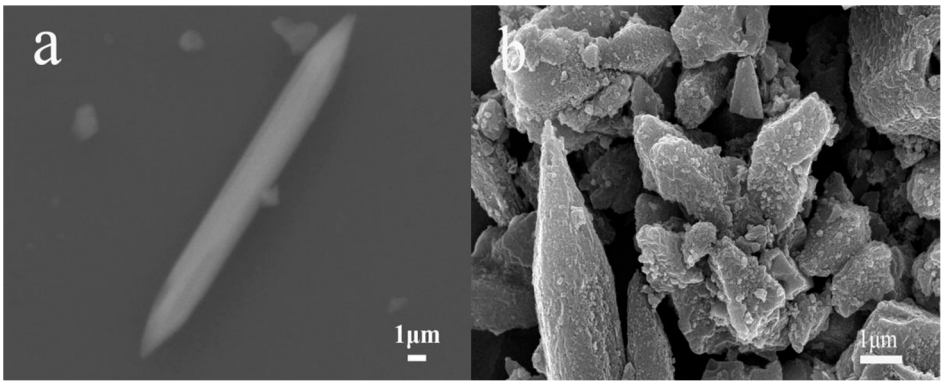

Figure 4. SEM images of (**a**) MIL-88D and (**b**) Fe_3O_4@C.

In order to further study the changes in its specific surface area and pore structure, N_2 adsorption and desorption isotherm tests were carried out on MIL-88D and the derived carbon-coated iron oxide composites. The specific results are shown in Figure 5. It can be seen that both materials exhibit type IV isotherms, indicating that the carbon-coated iron oxide composite prepared by this method retains the original MIL-88D structure. The corresponding specific surface area was calculated by BJH (as shown in Table 1). It was found that, after high-temperature treatment, the specific surface area decreased to a certain extent, but still maintained a high level. At 700 °C, the specific surface area was as high as 248.10 m^2/g. Meanwhile, the pore structures of the two materials were compared and analyzed. It was found that Fe_3O_4@C showed a single mesoporous characteristic with a pore size of 3.76 nm, which could be confirmed by SEM to a certain extent. The uniform distribution of mesoporous structures may be due to the uniform and dense arrangement of small protrusions on the surface, which is more conducive to the adsorption of heavy metal ions by the materials. It is worth noting that the pore structure characteristics can be verified by SEM.

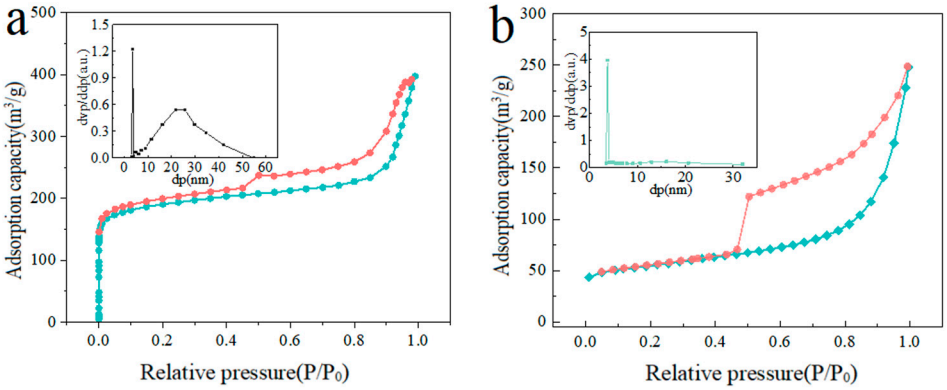

Figure 5. BET diagrams of (**a**) MIL-88D and (**b**) Fe_3O_4@C.

Table 1. Specific surface area and pore size of MIL-88D and its derived composites.

Sample	MIL-88D	Fe_3O_4@C
Specific surface area (m^2/g)	392.51	248.10
Aperture (nm)	3.64/21.73	3.76

In order to further investigate the separation effect of composite materials under an external magnetic field, the magnetic properties of Fe_3O_4@C were characterized. As can be seen from Figure 6, the hysteresis loop of Fe_3O_4@C is in the shape of an "S", and the saturation magnetization is as high as 19.13 emu/g. No coercive force or remanent magnetization occurs in the sample during magnetization, indicating that it has strong

superparamagnetism. The inset shows that Fe_3O_4@C can be rapidly adsorbed under an applied magnetic field, thus enabling the material to be efficiently separated from the water by an applied magnetic field.

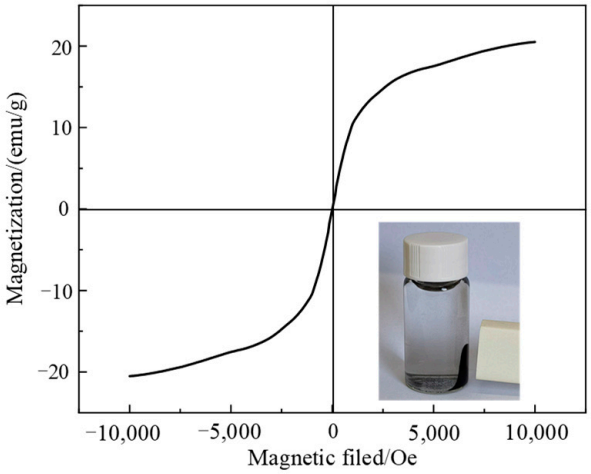

Figure 6. Hysteresis loop of Fe_3O_4@C (the inset is the separation effect of Fe_3O_4@C under an external magnetic field).

3.2. Adsorption Properties of Sample

The effect of different initial pH values on the adsorption effect was investigated under the condition of a 1 g/L addition of the derived porous carbon-coated iron oxide adsorbent, a 50 mg/L mass concentration of Cu^{2+}, and 2 h oscillation at room temperature, as shown in Figure 7a. MIL-88D(Fe) and its derivative Fe_3O_4@C have certain adsorption properties, but the adsorption capacity of Fe_3O_4@C is significantly higher than that of MIL-88D(Fe). Although MIL-88D(Fe) has certain adsorption properties due to its large specific surface area, its poor solubility in water is not suitable for practical application in the field of water treatment. The initial pH of the solution will affect the degree of protonation on the surface of the adsorption material, thus affecting the removal of heavy metal ions. When the initial pH of the solution is low, more H^+ in the system enhances the protonation degree of porous carbon-coated iron oxide, that is, in increases the electrostatic repulsion with positively charged Cu^{2+} and decreases its removal rate. When the initial pH value is increasing, the adsorption effect of Cu^{2+} is the best with the increase in OH^- content in the system. However, the pH value of the system is too high; although the apparent Cu^{2+} removal rate may be relatively high, the main reason is the formation of copper hydroxide precipitation in the alkaline environment. Therefore, under the condition of high pH, the efficiency of heavy metal ion removal will be significantly reduced due to the performance of the adsorbent itself. In order to explain the variation in the adsorption properties of Cu(II)with pH, the zeta potential and zero charge point pH_{PZC} of Fe_3O_4@C in the range of pH = 3–9 were further measured (Figure 7b). Relatively high pH_{PZC} values cause the sample to exhibit significant variable charge characteristics: trapping protons at pH levels below the zero charge point and introducing positive charges, and dissociating protons at higher pH values and introducing negative charges.

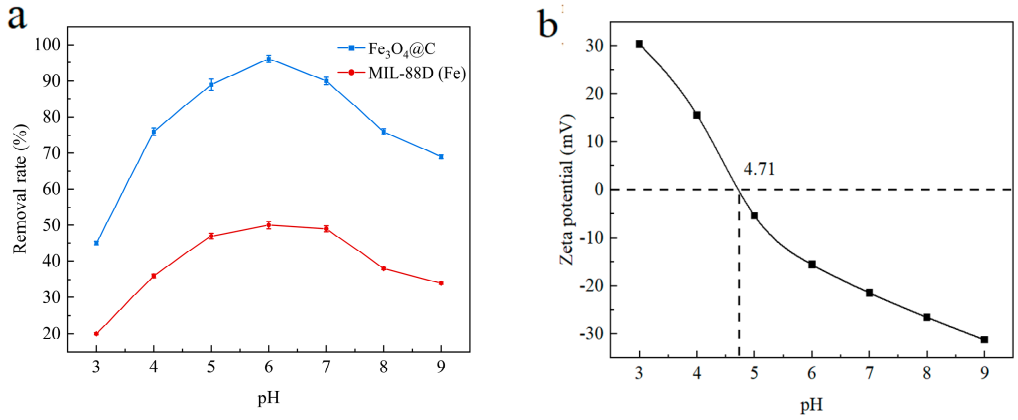

Figure 7. (**a**) Effect of initial pH value of solution on Cu^{2+} adsorption; (**b**) influence of pH on the zeta potential on Fe_3O_4@C.

The correlation between the Cu^{2+} adsorption capacity Q_e in the range of pH = 3–7 at Fe_3O_4@C and the corresponding zeta potential was analyzed, and both showed a good correlation (R^2 = 0.84). This indicates that the pH-dependent Cu^{2+}-adsorption behavior of Fe_3O_4@C is closely related to its surface variable charge. It is, further, proved that, in the low-pH region, the surface of Fe_3O_4@C has a net positive charge and forms electrostatic repulsion with Cu^{2+}, which is not conducive to Fe_3O_4@C adsorption of Cu^{2+}. In the high-pH region, the surface of Fe_3O_4@C has a net negative charge, which forms electrostatic attraction to Cu^{2+} and shows a higher adsorption removal of Cu^{2+}.

As can be seen from Figure 8, when the adsorbent is adsorbed for 10 min, there is a large number of empty adsorption sites on the surface of the adsorbent, and the removal rate of Cu^{2+} by porous carbon coated with iron oxide can reach 90%. With the extension of the adsorption time, the adsorption site is gradually occupied by metal ions, the electrostatic repulsion between metal ions in the adsorption phase and metal ions in the solution phase is enhanced, and the concentration difference (driving force) of solute diffusion to the surface of the adsorbent is decreased, resulting in difficulty in later adsorption and the adsorption rate gradually slowing down. After 30 min, the adsorption curve of the porous carbon-coated iron oxide on Cu^{2+} gradually flattened, that is, a dynamic equilibrium process of adsorption and desorption was achieved.

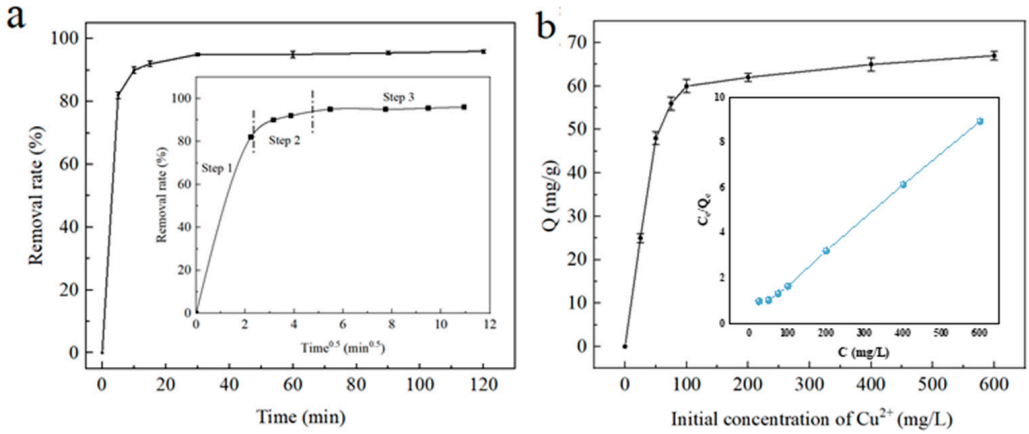

Figure 8. Cu^{2+} adsorption: (**a**) the effect of adsorption time (the inset is the fitting of adsorption diffusion process); (**b**) the effect of initial concentration (the inset is the fitting of Langmuir model).

The experimental data were simulated for adsorption first-order kinetics and second-order kinetics [23], and the calculation results are shown in Table 2. It can be seen from Table 2 that the second-order kinetic equation can well-describe the adsorption process of Cu^{2+} by porous carbon-coated iron oxide, with the adsorption rate constant k_2 being

0.0076 g/(mg·min) and the R^2 being 0.9977, indicating that the adsorption is mainly controlled by chemical action rather than by material transport steps. The mass-transfer mechanism of Cu(II) adsorbed by Fe_3O_4@C was further investigated by using the intraclass diffusion model. The relevant results are shown in the illustrations in Figure 8a. It can be seen from the figure that Cu(II) at Fe_3O_4@C first diffuses externally in the liquid film around the Fe_3O_4@C. Next is internal diffusion in the Fe_3O_4@C mesopore; finally, there is adsorption at the active site Fe_3O_4@C. Moreover, the fitting line of step 1 passes through the origin, which indicates that intra-particle diffusion is involved as a rate control step in the initial stage of adsorption. However, the fitting lines for steps 2 and 3 do not pass through the origin, suggesting that intra-particle diffusion is not the only rate-determining step in the adsorption process, and that chemisorption mechanisms may also be involved.

Table 2. The fitting results of adsorption kinetic parameters.

First-Order Kinetic Equation		Second-Order Kinetic Equation	
Q_e (mg/g)	56.61	Qe (mg/g)	52.91
k_1 (min^{-1})	0.0466	k_2 (g/mg·min)	0.0076
R^2	0.7911	R^2	0.9977

It can be seen from Figure 8b that the adsorption isotherm of porous carbon-coated iron oxide for Cu^{2+} is L-shaped. With the increase in the initial mass concentration of Cu^{2+}, the adsorption capacity also increases. The adsorption capacity will increase rapidly with the increase in the equilibrium mass concentration of metal ions in the solution. Even in the solution with a low mass concentration, there is a strong adsorption of heavy metal ions, and a better removal rate can be achieved with less cellulose, which is conducive to the full utilization of the adsorbent. As the concentration of the solution increases to a certain extent, the content of heavy metal ions in the solution and the exchange site of the adsorption material gradually decrease, making the slope of the isotherm decrease and tend to be gentle until the adsorption amount tends to a constant value, thus achieving adsorption equilibrium.

After fitting the relationship between the adsorption capacity and initial mass concentration of heavy metal ions (Cu^{2+}) by porous carbon coated with iron oxides, the adsorption parameters and correlation coefficient R are shown in Table 3 [24]. As can be seen from Table 3, the fitting results are obviously in line with the Langmuir (R^2 = 0.9981) adsorption model, reaching a very significant level, indicating that the adsorption of heavy metal ions (Cu^{2+}) by porous carbon-coated iron oxides is done by a single molecular layer. Based on the fitting of the Langmuir adsorption isothermal model, the adsorption strength (R_L) can be further calculated according to the kL value of the Langmuir constant at a certain temperature, that is, $R_L = 1/(1 + k_L C_0)$. It is generally believed that, when $0 < R_L < 1$, ions in solution are easily adsorbed; on the contrary, when $R_L > 1$, ions in the solution are not easily adsorbed [25]. As can be seen from Table 3, k_L is a positive number, so the adsorption strength of porous carbon-coated iron oxides on metal ions is less than 1, and the RL also decreases with the increase in the initial mass concentration of heavy metal ions (Cu^{2+}), which fully indicates that, the greater the initial mass concentration of heavy metal ions, the more favorable the adsorption [26].

Table 3. The fitting results of adsorption isotherm model parameters.

Langmuir Adsorption Isotherm		Freundlich Adsorption Isotherm	
Q_e (mg/g)	69.93	n	0.2473
k_L (L/mg)	0.0378	k_F (L/g)	15.92
R^2	0.9981	R^2	0.6665

In Table 4, the Fe_3O_4@C composite adsorbent prepared in this experiment is compared with several other representative Cu^{2+} adsorbents. As can be seen from the table, the adsorption capacity of the Fe_3O_4@C composite for Cu^{2+} is higher than that of other materials. This is mainly due to the micropore-filling and electrostatic action of porous carbon in Fe_3O_4@C composite.

Table 4. Comparison of adsorption capacities of different adsorbents for Cu^{2+}.

Adsorbent	Adsorption Apacity (mg/g)	Cite Literature
Fe_3O_4@C	69.93	This work
pectin β-cyclodextrin composite	12.51	[27]
Cellulose reinforced electrospunchitosan nanofibers	36.76	[28]
SiO_2-TEPA-NA	13.44	[29]
The adsorbent prepared from Bayer's method-derived red mud (RM)	68.86	[30]
Magnetically modified iron oxide immobilized biochar adsorbent using Juglans regia shells	16.83	[31]
Chlorides-modified hydrochars	54.74	[32]

3.3. Reusability of Fe_3O_4@C

The reuse performance of the adsorbent is another important indicator to realize its potential application in practical wastewater treatment. Therefore, the adsorption and desorption cycle experiments of Fe_3O_4@C for the adsorption properties of Cu^{2+} ions were carried out at room temperature. As can be seen from the experimental results in Figure 9a, the composite still showed an excellent adsorption capacity for heavy metal Cu^{2+} ions after desorption in EDTA (0.1M) solution. In particular, the removal rate of heavy metal Cu^{2+} ions by Fe_3O_4@C remained at nearly 80% of the initial adsorption value after five cycles. The slight decrease in the adsorption capacity of the composite after cyclic adsorption may be due to the decrease in the active site and the plugging of porous carbon pores in several aspects [26]. On the one hand, the content of residual heavy metal ions in the adsorbent gradually increases, which reduces the amount of exposed active sites. On the other hand, the products formed by chemisorption and complexation adhere to the surface of the adsorbent, which not only reduces the number of active sites on the surface of the adsorbent, but also blocks the pores of porous carbon, which reduces the mass-transfer capacity of the heavy metal ions.

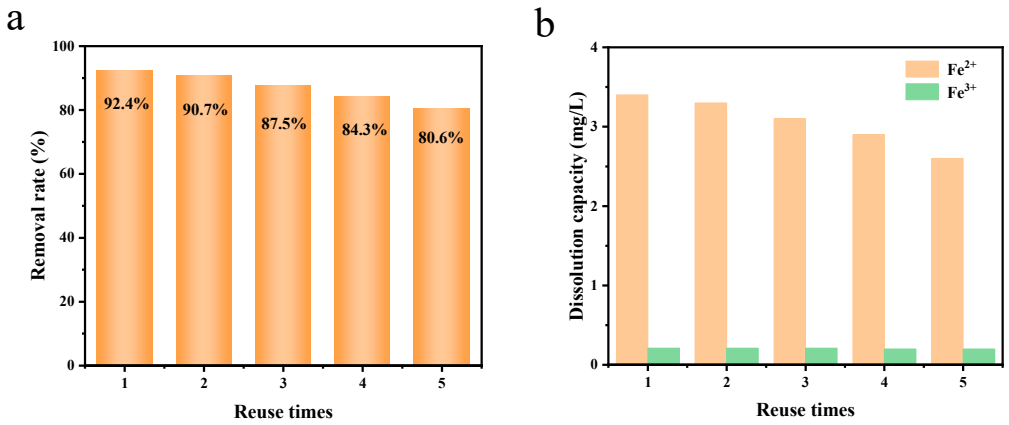

Figure 9. The adsorption capacity of Cu^{2+} (**a**); the dissolution capacity of Fe^{2+} and Fe^{3+} in the recycling experiment (**b**).

In order to further investigate the stability of Fe_3O_4@C, the dissolution of Fe^{2+} and Fe^{3+} after adsorption was detected simultaneously. Figure 8b shows the change in the amount of Fe^{2+} and Fe^{3+} dissolved during the reuse process. The solubility of Fe^{2+} and Fe^{3+} in each copper ion adsorption process is lower than 0.2 mg/L, which fully indicates

that the Fe_3O_4@C adsorption material is very stable during the adsorption of copper ions, and that dissolved ions will not cause secondary pollution to the environment. After each adsorption of copper ions, the dissolution amount of bivalent iron ions decreases with the decrease in the adsorption amount of copper ions, and the dissolution amount of trivalent iron ions does not decrease significantly, indicating that the main adsorption process of the adsorption of copper ions by the adsorption material is the exchange of bivalent iron ions with copper ions, supplemented by the exchange of trivalent iron ions with copper ions [27,28].

3.4. Adsorption Mechanism of Fe_3O_4@C

Further, combined with previous characterization results of surface functional groups, the specific surface area of magnetic porous carbon composites, and experimental results of adsorption of Cu^{2+}, the main adsorption mechanisms of Cu^{2+} by Fe_3O_4@C include ion exchange, pore diffusion, electrostatic action, and coordination action, as shown in Figure 10 [33,34].

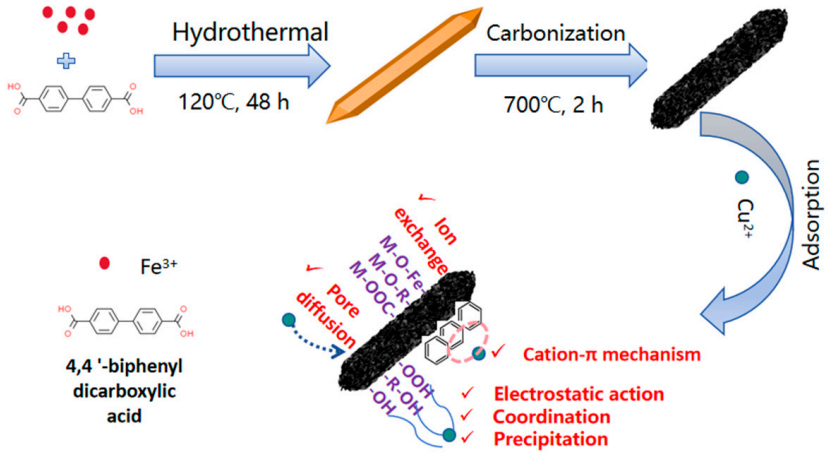

Figure 10. Schematic diagram of material synthesis and adsorption mechanism.

Firstly, the charged cation in Fe_3O_4@C can dissolve and have ion exchange with Cu(II). In the above experiments, the concentration of Fe^{2+} ions in the supernatant after the adsorption of Cu^{2+} is significantly increased [35]. Secondly, the high specific surface area and developed pore structure of Fe_3O_4@C not only strengthen the contact between the adsorption site on the surface of porous carbon and the heavy metal ions, but also enhance the contact between the adsorption site on the surface of porous carbon and the heavy metal ions, which is conducive to the introduction of new functional groups. The adsorption kinetics of Cu(II) and the rapid initial adsorption of the Fe_3O_4@C adsorption isotherm are attributed to pore diffusion [36,37]. Thirdly, electrostatic action is one of the main mechanisms affecting the removal of Cu(II) from Fe_3O_4@C. The negative charge on the porous carbon surface easily interacts with Cu(II). The functional groups on the porous carbon surface are important factors affecting the electrostatic action. Under different pH levels, the functional groups show different chemical forms, thus affecting the electrostatic action. Charged Fe_3O_4@C has an electrostatic adsorption effect on heavy metal ions, limiting the free state of the heavy metal ions. Therefore, the carbonization temperature is the main factor affecting the electrostatic interaction of functional groups on the surface of porous carbon [38]. Finally, coordination is the main mechanism of removing Cu(II) from magnetic porous carbon material (Fe_3O_4@C), because Cu(II) has a strong coordination ability and can form adsorption sites with carboxyl, hydroxyl, and other functional groups contained in porous carbon, and coordination between these adsorption sites and metal ions occurs [39].

4. Conclusions

In this paper, the magnetic porous carbon composite Fe_3O_4@C was synthesized by hydrothermal recombination and the carbonization of the fusiform MIL-88D (Fe) as the precursor. The material still maintains the frame structure of MIL-88D (Fe), the central ion Fe is oxidized into nanometer iron oxide with magnetic properties, which is evenly distributed in the carbon-based pores, and the composite adsorption material of iron oxide and porous carbon is obtained. After carbonization, the original smooth spindle structure became rough, and the number of active sites increased. At the same time, the magnetic ferric oxide formed under the action of an external magnetic field is conducive to realizing fast solid–liquid separation. Compared with pure MIL-88D (Fe), the adsorption capacity of the Fe_3O_4@C material for Cu^{2+} ions is greatly improved. The pH value is an important parameter that affects the adsorption effect. When the pH is 6 and the adsorption time is 30 min, the adsorption effect is the best, and the removal rate is 96%. The adsorption process of Cu^{2+} by porous carbon-coated iron oxide conforms to the second-order reaction kinetics and Langmuir adsorption isothermal equation, indicating that the adsorption process occurs mainly through chemisorption and typical single-molecular-layer adsorption.

Author Contributions: Conceptualization and methodology, Z.Z. and J.Y.; formal analysis, investigation, and data curation J.Y., Z.Z. and L.J.; writing—original draft preparation, L.J.; writing—review and editing, J.Z., Z.Z., L.J. and M.L. All authors have read and agreed to the published version of the manuscript.

Funding: This project was supported financially by the National Natural Science Foundation of China (No. 51672040) and Science and Technology Research Projects of the Education Department of Jilin Province (No. JJKH20180429KJ).

Data Availability Statement: The raw data supporting the conclusions of this article will be made available by the authors on request.

Acknowledgments: The authors extend their gratitude to Zhu Yao from Shiyanjia Lab (www.shiyanjia.com) for providing invaluable assistance with the SEM analysis.

Conflicts of Interest: Authors Zhongyuan Zheng, Jinshan Yu, Ling Jiang and Jiacheng Zhang were employed by State Grid Tianjin Electric Power Company Electric Power Science Research Institute. The remaining author declares that the research was conducted in the absence of any commercial or financial relationships that could be construed as a potential conflict of interest.

References

1. Yagub, M.T.; Sen, T.K.; Afroze, S.; Ang, H.M. Dye and its removal from aqueous solution by adsorption: A review. *Adv. Colloid Interface* **2014**, *209*, 172–184. [CrossRef]
2. Ahmad, A.; Mohd-Setapar, S.H.; Chuong, C.S.; Khatoon, A.; Wani, W.A.; Kumar, R.; Rafatullah, M. Recent advances in new generation dye removal technologies: Novel search for approaches to reprocess wastewater. *RSC Adv.* **2015**, *5*, 30801–30818. [CrossRef]
3. Gao, Q.; Xu, J.; Bu, X.-H. Recent advances about metal–organic frameworks in the removal of pollutants from wastewater. *Coord. Chem. Rev.* **2019**, *378*, 17–31. [CrossRef]
4. Savage, N.; Diallo, M.S. Nanomaterials and water purification: Opportunities and challenges. *J. Nanopart. Res.* **2005**, *7*, 331–342. [CrossRef]
5. Haque, E.; Lee, J.E.; Jang, I.T.; Hwang, Y.K.; Chang, J.-S.; Jegal, J.; Jhung, S.H. Adsorptive removal of methyl orange from aqueous solution with metal-organic frameworks, porous chromium-benzenedicarboxylates. *J. Hazard. Mater.* **2010**, *181*, 535–542. [CrossRef]
6. Sun, L.; Wang, J.; Wu, J.; Wang, T.; Du, Y.; Li, Y.; Li, H. Constructing nanostructured silicates on diatomite for Pb(II) and Cd(II) removal. *J. Mater. Sci.* **2019**, *54*, 6882–6894. [CrossRef]
7. Bulut, Y.; Karaer, H. Adsorption of Methylene Blue from aqueous solution by crosslinked chitosan/bentonite composite. *J. Disper. Sci. Technol.* **2014**, *36*, 61–67. [CrossRef]
8. Li, Y.; Li, J.; Wang, L.; Zhou, B.; Chen, Q.; Bu, X. Microporous metal–organic frameworks with open metal sites as sorbents for selective gas adsorption and fluorescence sensors for metal ions. *J. Mater. Chem. A* **2013**, *1*, 495–499. [CrossRef]
9. Wu, Y.; Zhou, M.; Li, S.; Li, Z.; Li, J.; Wu, B.; Li, G.; Li, F.; Guan, X. Magnetic metal–organic frameworks: γ-Fe_2O_3@MOFs via confined in situ pyrolysis method for drug delivery. *Small* **2014**, *10*, 2927–2936. [CrossRef]

10. Mohamed, E.; Jaheon, K.; Nathaniel, R.; David, V.; Joseph, W.; Michael, O.; Yaghi, O. Systematic design of pore size and functionality in isoreticular MOFs and their application in methane storage. *Science* **2002**, *295*, 469–472.
11. Xu, Y.; Jin, J.; Li, X.; Han, Y.; Meng, H.; Song, C.; Zhang, X. Magnetization of a Cu(II)-1,3,5-benzenetricarboxylate metal-organic framework for efficient solid-phase extraction of Congo Red. *Microchim. Acta* **2015**, *182*, 2313–2320. [CrossRef]
12. Li, Z.; Yang, J.; Sui, K.-W.; Yin, N. Facile synthesis of metal-organic framework MOF-808 for arsenic removal. *Mater. Lett.* **2015**, *160*, 412–414. [CrossRef]
13. Liu, X.; Wang, C.; Wu, Q.; Wang, Z. Metal-organic framework-templated synthesis of magnetic nanoporous carbon as an efficient absorbent for enrichment of phenylurea herbicides. *Anal. Chim. Acta* **2015**, *870*, 67–74. [CrossRef] [PubMed]
14. Feng, Y.; Amatjan, S.; Rena, S.; Xieraili, M.; Jiao, X. In situ self-assembly of ZIF-8@sodium alginate composite hydrogels for enhanced adsorption of Cu^{2+} ions. *Colloids Surfaces A* **2024**, *702*, 135040. [CrossRef]
15. Xu, D.; Qin, Y.; Cao, X.; Huang, Y.; Wang, J.; Liu, X.; Liu, F.; Li, X. Study on the adsorption of Ce(III) on phosphonic acid functionalized ZIF-67@SiO_2 magnetic porous carbon materials. *Colloids Surfaces A* **2024**, *696*, 134306. [CrossRef]
16. Liang, R.; Chen, R.; Jing, F.; Qin, N.; Wu, L. Multifunctional polyoxometalates encapsulated in MIL-100(Fe): Highly efficient photocatalysts for selective transformation under visible light. *Dalton Trans.* **2015**, *44*, 18227–18236. [CrossRef]
17. Liang, C.; Meng, Y.; Lu, M.; Wang, G. Insights into the impact of interlayer spacing on MXene-based electrodes for supercapacitors: Areview, J. *Energy Storage* **2023**, *65*, 107341. [CrossRef]
18. Wei, Z.; Xing, R.; Zhang, X.; Liu, S.; Yu, H.; Li, P. Facile Template-Free Fabrication of Hollow Nestlike α-Fe_2O_3 Nanostructures for Water Treatment. *ACS Appl. Mater. Interfaces* **2012**, *5*, 598–604. [CrossRef]
19. Huang, Y.-H.; Hsueh, C.-L.; Cheng, H.-P.; Su, L.-C.; Chen, C.-Y. Thermodynamics and kinetics of adsorption of Cu(II) onto waste iron oxide. *J. Hazard. Mater.* **2007**, *144*, 406–411. [CrossRef]
20. Bara, D.; Wilson, C.; Mörtel, M.; Khusniyarov, M.M.; Ling, S.; Slater, B.; Sproules, S.; Forgan, R.S. Kinetic control of interpenetration in Fe–biphenyl-4,4′-dicarboxylate metal–organic frameworks by coordination and oxidation modulation. *J. Am. Chem. Soc.* **2019**, *141*, 8346–8357. [CrossRef]
21. Lin, X.; Chen, P.; Fenghua, H. Effect of SiO_2 surface coating on the properties of Fe_3O_4 magnetic microspheres. *Chin. J. Synth. Chem.* **2010**, *18*, 507–510.
22. Luo, X.; Ding, L.; Luo, J. Adsorptive removal of Pb(II) ions from aqueous amples with amino-functionalization of metal–organic frameworks MIL-101(Cr). *J. Chem. Eng. Data* **2015**, *60*, 1732–1743. [CrossRef]
23. Lu MLv, X.; Xu, X.; Tingting, G. Study on the adsorption mechanism of amphoteric bacterial cellulose to persistent pollutants. *J. Funct. Mater.* **2014**, *23*, 23054–23058.
24. Abdelghani, H.; Redouane, H.; Abdelaziz, I.; Yassine, N.; Rahime, E.; Abdelillah, S.; Sabine, S.; Rabah, B.; Abdallah, A. 1,2,4,5-benzene tetracarboxylic acid-doped polyaniline/protonated carbon nitride nanostructures for Cr(VI) adsorption in water. *ACS Appl. Nano Mater.* **2024**, *7*, 13050–13061.
25. Ye, M.; Zou, J.; Chen, D.; Song, Y.; Sun, Y.; Guo, C. Preparation of Tobermolite based on two typical solid wastes and its adsorption properties for Cd^{2+}. *J. Chin. Coal Soc.* **2023**, *48*, 3289–3299.
26. Li, S. Study on the Remediation of Nickel-Contaminated Soil by Rhamnose-Lipid-Modified Nano Zero-Valent Iron and Its Mechanism. Master's Thesis, East China University Of Science and Technology, Shanghai, China, 2021.
27. Fu, M.; Tuo, X.; Yan, X.; Li, D.; Zhu, H.; Gao, S.; Han, X.; Zhou, J.; Mou, D.; Xiu, J. Adsorption performance and mechanism of pectin modified with β-cyclodextrin for Zn^{2+} and Cu^{2+}. *Int. J. Biol. Macro. Mol.* **2024**, *274*, 133563. [CrossRef]
28. Bates, I.I.C.; Loranger, E.; Mathew, A.P.; Chabot, B. Cellulose reinforced electrospun chitosan nanofibers bio-based composite sorbent for water treatment applications. *Cellulose* **2021**, *28*, 4865–4885. [CrossRef]
29. Wang, M.; Wang, A.; Cai, H.; Niu, Y. Preparation of polyamine grafted silica gels supported naphthaldehyde Schiff's base and their adsorption properties as Cu^{2+} ions adsorbents. *Desalin. Water Treat.* **2021**, *226*, 208–222. [CrossRef]
30. Yang, X.; Li, C.; Ma, W.; Li, J.; Feng, S.; Zhang, L.; Mao, A. Study on the adsorption performance of Cu^{2+} in wastewater by red mud. *Desalin. Water Treat.* **2024**, *317*, 100524–100531. [CrossRef]
31. Runit, I.; Shaziya, S.; Obaid, F.; Mohammad, K. Magnetic biochar derived from Juglans regia for the adsorption of Cu^{2+} and Ni^{2+}: Characterization, modelling, optimization, and cost analysis. *J. Saudi Chem. Soc.* **2023**, *27*, 101749–101764.
32. Yang, R.; Feng, S.; Jin, D.; Wang, Y.; Li, D.; Liang, Y.; Wu, J. Removing DOM from chloride modified hydrochar could improve Cu^{2+} adsorption capacity from aqueous solution. *Chemosphere* **2023**, *342*, 140202–140213. [CrossRef] [PubMed]
33. Zhang, L.; Li, W.; Cao, H.; Hu, D.; Chen, X.; Guan, Y.; Tang, J.; Gao, H. Ultra-efficient sorption of Cu^{2+} and Pb^{2+} ions by light biochar derived from Medulla tetrapanacis. *Bioresour. Technol.* **2019**, *291*, 121818. [CrossRef] [PubMed]
34. Xing, Y.; Liu, S.; Wang, W.; Liang, Y.; Fu, J.; Zhou, Q.; Wang, L.; Huang, S. Synergistic effects of aluminum doping and amino functionalization to enhance adsorption capacity of ultrathin-nanosheet-assembled calcium silicate hydrate architectures for effective removal of Pb^{2+} and Cu^{2+} from aqueous solution. *J. Environ. Chem. Eng.* **2024**, *12*, 112194–112207. [CrossRef]
35. Chen, Y.; Li, M.; Li, Y.; Liu, Y.; Chen, Y.; Li, H.; Li, L.; Xu, F.; Jiang, H.; Chen, L. Hydroxyapatite modified sludge-based biochar for the adsorption of Cu^{2+} and Cd^{2+}: Adsorption behavior and mechanisms. *Bioresour. Technol.* **2021**, *321*, 124413. [CrossRef]
36. Yu, C.; Wang, M.; Dong, X.; Shi, Z.; Zhang, X.; Lin, Q. Removal of Cu (ii) from aqueous solution using Fe_3O_4–alginate modified biochar microspheres. *RSC Adv.* **2017**, *7*, 53135–53144. [CrossRef]

37. Deng, J.; Li, X.; Wei, X.; Liu, Y.; Liang, J.; Tang, N.; Song, B.; Chen, X.; Cheng, X. Sulfamic acid modified hydrochar derived from sawdust for removal of benzotriazole and Cu (II) from aqueous solution: Adsorption behavior and mechanism. *Bioresour. Technol.* **2019**, *290*, 121765. [CrossRef] [PubMed]
38. Mei, Y.; Li, B.; Fan, S. Biochar from rice straw for Cu^{2+} removal from aqueous solutions: Mechanism and contribution made by acid-soluble minerals. *Water Air Soil Poll.* **2020**, *231*, 420. [CrossRef]
39. Liu, J.; Liu, H.; Yang, X.; Jia, X.; Cai, M.; Bao, Y. Preparation of Si-Mn/biochar composite and discussions about characterizations, advances in application and adsorption mechanisms. *Chemosphere* **2021**, *281*, 130946. [CrossRef]

Disclaimer/Publisher's Note: The statements, opinions and data contained in all publications are solely those of the individual author(s) and contributor(s) and not of MDPI and/or the editor(s). MDPI and/or the editor(s) disclaim responsibility for any injury to people or property resulting from any ideas, methods, instructions or products referred to in the content.